
Article:

Giorgi, M. orcid.org/0000-0001-7763-8545 and Dall'Ara, E. orcid.org/0000-0003-1471-5077 (2018) Variability in strain distribution in the mice tibia loading model: A preliminary study using digital volume correlation. Medical Engineering and Physics, 62. pp. 7-16. ISSN 1350-4533

https://doi.org/10.1016/j.medengphy.2018.09.001

Medical Engineering and Physics 62 (2018) 7–16

Contents lists available at ScienceDirect

Medical Engineering and Physics

journal homepage: www.elsevier.com/locate/medengphy

Variability in strain distribution in the mice tibia loading model: A preliminary study using digital volume correlation

M. Giorgi [a,b,c,*], E. Dall'Ara [a,b]

[a] Department of Oncology and Metabolism, Mellanby Centre for Bone Research, University of Sheffield, UK
[b] INSIGNEO Institute for in Silico Medicine, University of Sheffield, UK
[c] Certara QSP, Certara UK Limited, Simcyp Division, Sheffield, UK

ARTICLE INFO

Article history:
Received 25 October 2017
Revised 28 June 2018
Accepted 2 September 2018

Keywords:
Digital volume correlation (DVC)
Mouse tibia
Strain variability
microCT
In vivo µCT
Ex vivo µCT
In situ µCT

ABSTRACT

It is well known that bone has an enormous adaptive capacity to mechanical loadings, and to this extent, several *in vivo* studies on mouse tibia use established cyclic compressive loading protocols to investigate the effects of mechanical stimuli. In these experiments, the applied axial load is well controlled but the positioning of the hind-limb between the loading endcaps may dramatically affect the strain distribution induced on the tibia. In this study, the full field strain distribution induced by a typical *in vivo* setup on mouse tibiae was investigated through a combination of *in situ* compressive testing, µCT scanning and a global digital volume correlation (DVC) approach. The precision of the DVC method and the effect of repositioning on the strain distributions were evaluated. Acceptable uncertainties of the DVC approach for the analysis of loaded tibiae (411 ± 58με) were found for nodal spacing of approximately 50 voxels (520 µm). When pairs of *in situ* preloaded and loaded images were registered, low variability of the strain distributions within the tibia were seen (range of mean differences in principal strains: 585–1800με). On contrary, larger differences were seen after repositioning (range of mean differences in principal strains: 2500–5500με). To conclude, these preliminary results on thee specimens showed that the DVC approach applied to the mouse tibia can be precise enough to evaluate local strain distributions under loads, and that repositioning of the hind-limb within the testing machine can induce large differences in the strain distributions that should be accounted for when modelling this system.

1. Introduction

There is much experimental evidence of bone adapting its mass and structure to different loading conditions following mechanotransduction (net bone resorption occurring at low strains and net bone formation occurring at high strains or micro-damage theories [1–9]). However, the mechanisms are still unclear, and a comprehensive understanding about how loads impact the bone remodelling process is required in order to improve diagnostic methods and treatments for bone pathologies. Mice models are used intensively for investigating the impact of mechanical stimuli on bone remodelling in the mouse tibia [10–14] by studying bone response to physiological (*e.g.*,. running on treadmill) [15,16] and para-physiological [11–13] loading conditions. In the former case it is difficult, if not impossible to control the applied load during activities. In the latter, a passive axial compression of the mouse tibia is applied through the ankle and the knee joints. By using this configuration, several studies assessed bone response on mouse tibia to well defined cyclic compressive loading *in vivo* by varying, for example, the peak loads, waveforms, frequency and number of cycles [6,12,13,17–21].

However, these experimental measurements are not trivial for mice bones, due to the difficult control of the positioning of the hind-limb between the loading endcaps (at the knee and ankle). In fact, while in such experiments the applied axial load is well controlled, the distribution of strains induced on the tibia through the joints, depends on the relative position of the bones and may differ from one loading session to another, or among animals. Therefore, we need to measure more effectively the variability of strain distribution induced by the loading procedure. Strain gauges [22,23] can be used for local measurements of strain, but are disputed for several reasons: possible reinforcement effects for small structures like the mouse tibia, averaging properties over a large surface, and are limited to a few discrete measurements [24,25]. Digital image correlation (DIC) techniques have been used to measure strains on deforming mice bones [26,27]. However, while DIC can pro-

* Corresponding author at: Department of Oncology and Metabolism, Mellanby Centre for Bone Research, University of Sheffield, UK.
E-mail address: mario.giorgi@certara.com (M. Giorgi).

https://doi.org/10.1016/j.medengphy.2018.09.001
1350-4533/

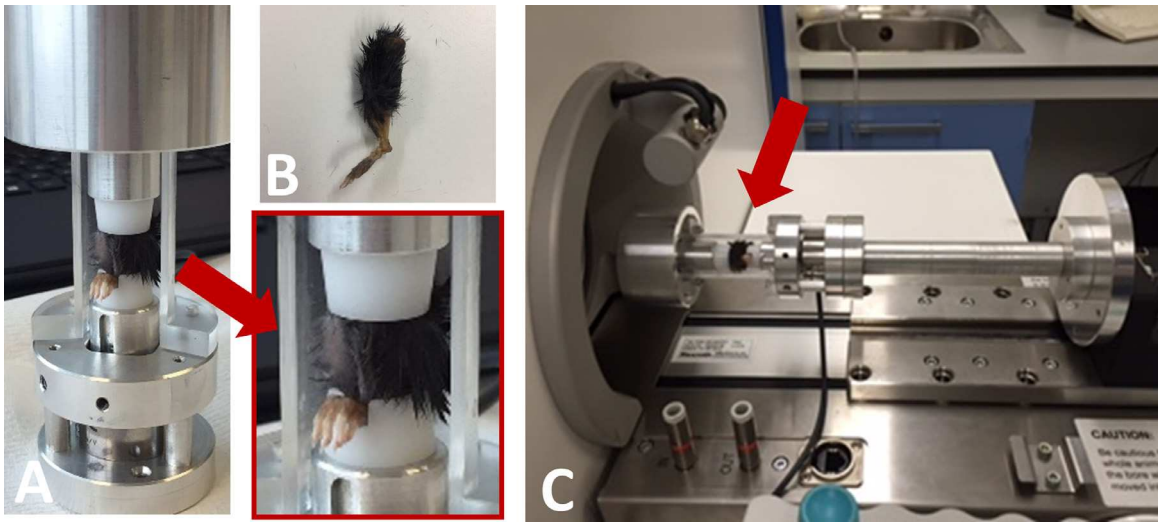

Fig. 1. (A) Custom-made loading device used for *in situ* scans with zoomed region where the lower limb is placed (red box); (B) example of lower limb used for *in situ* scanning which has been surgically detached from the mouse body; (C) example of the *in situ* custom-made loading device within the µCT system (red arrow).

vide spatially richer information compared with strain gauges, it is restricted to a portion of the external bone surface, missing the potential of exploring the strain distribution within the bone due to microstructural heterogeneity [25,28]. Recently, digital volume correlation (DVC) applied to µCT images of specimens scanned in un-deformed and deformed configurations has been used to estimate the internal displacements and strain distribution of trabecular bone specimens extracted from human or animal tissue [29–32], cortical bone from the mid-diaphysis of mice femora [33], and on whole human [34] or porcine [35] vertebral bodies. For every new DVC application, it is fundamental to carefully measure the precision of the technique before any direct application [36]. This evaluation can be performed either with repeated scan measurements in zero-strain condition [37–39], which account for the image noise, or by registering virtually stretched images [33], which probably underestimates the uncertainties due to the absence of the image noise [38]. To the best of the authors' knowledge, nobody has evaluated the precision of the DVC for bone applications under loading, and at the same time accounted for the image noise. Moreover, no DVC studies have been reported on the estimation of internal strain of the whole mouse tibia under controlled loads.

The aim of this study is to investigate the variability in the full field strain distribution induced by the same loading conditions of *in vivo* loading experiments of the mouse tibia. In order to achieve this goal, in this study, the precision error of a global DVC approach for investigation of local strains was initially assessed on the whole mouse tibia in preloaded and loaded conditions *in situ*, and then the effect of repositioning on the strain distribution was evaluated. In addition, the precision error of this DVC technique was also evaluated in zero-strain (unloaded) *ex vivo* and *in vivo* conditions (see supplementary materials).

2. Materials and methods

2.1. Specimens and scanning

Three mice (C57BL/6J, female, 22-weeks-old) tibiae collected from a previous study [40] were scanned *in situ* (legs isolated and placed in a custom made jig). Each tibia was scanned five times in preloaded and loaded conditions (see below for details). Each specimen was scanned [40] by using an *in vivo* µCT system (vivaCT 80, Scanco Medical, Bruettisellen, Switzerland) with the following scanning parameters: voltage of 55 keV, intensity of 145 µA, integration time of 200 ms, nominal isotropic image voxel size of 10.4 µm for a total scanning time of approximately 40 minutes per scan. Beam hardening artefacts were reduced by applying a third-order polynomial correction algorithm provided by the manufacturer based on scans of 1200 mgHA/cm^3 wedge phantom. All procedures were approved by the local Research Ethics Committee of the University of Sheffield (Sheffield, UK).

2.1.1. In situ *scans*

In order to evaluate the precision and accuracy of the DVC under compressive loads, a custom-made loading device that fits within the µCT system was designed. The jig was used to apply a controlled axial compression load between the knee and ankle joints (Fig. 1(A) and (C)), reproducing the typical boundary conditions of *in vivo* compression experiments of the mouse tibia used to study bone remodelling and mechano-regulation [23]. Three right lower limbs were detached from three mice surgically by dislocating the femur from the pelvis (Fig. 1(B)). A 100 N load cell (C9C, HBM, United Kingdom; accuracy class 0.2) was used to measure the compressive axial load, applied quasi-statically with a screw-ball joint. Each specimen was scanned five times: twice after the application of a preload (0.5 N; later referred to as "Preloaded1" and "Preloaded2") without repositioning in between the scans, twice after the application of a load (13 N, typically used for *in vivo* loading protocols [23]; later referred to as "Loaded1" and "Loaded2") without repositioning between the scans, and once in a loaded configuration after repositioning the specimen (13 N; later referred to as "Repositioned") for simulating what would happen *in vivo* between two loading sessions. At least 30 min were waited after the application of the load step in order to allow for the relaxation of the tissues. These scans were used to evaluate the precision of DVC in constant strain conditions by registering the repeated preloaded (RegP: Preloaded1 registered with Preloaded2, Table1) and repeated loaded (RegL: Loaded1 registered with Loaded2, Table1) scans. Moreover, to evaluate the variability in the distribution of the strain when the same specimen is loaded twice, a preloaded scan was registered with both loaded scans before (Reg2: Preloaded2 registered with Loaded2, Table1) and after (Reg3: Preloaded2 registered with Repositioned, Table1) repositioning. In order to investigate the strain variability between the two loaded conditions (before and after repositioning), the same preloaded set of images was used to minimise the effect

Table 1.
Summary of all preformed registrations.

Sample	Test	Registration	Image1	Image2	Repositioning	Rigid Reg.	NS	Output	Sample size
In situ	Constant strain Loaded	RegP	Preloaded1	Preloaded2	No	Yes	10–150	Prec. error	3
	Constant strain Loaded	RegL	Loaded1	Loaded2	No	Yes	10–150	Prec. error	3
	Strain distribution	Reg1	Preloaded2	Loaded1	No	Yes	50	Strain distr.	3
	Strain distribution	Reg2	Preloaded2	Loaded2	No	Yes	50	Strain distr.	3
	Variability strain distribution	Reg3	Preloaded2	Repositioned	Yes	Yes	50	Strain distr.	3

of image noise and interpolation. The deformable registration approach will account for potential rigid body motion between the preloaded condition before and after the repositioning, and the effect of repositioning on the strain distribution was computed (see Section 2.2 for details).

2.2. DVC protocol

After image reconstruction, each pair of images were first, rigidly registered using AMIRA software with normalised mutual information metric, and then a deformable image registration algorithm (ShIRT – Sheffield Image Registration toolkit [41–43] was used to compute the displacements at the nodes of an isotropic grid with selectable nodal spacing (NS) superimposed to the images. Since it has been shown that NS affects nonlinearly the DVC strain measurement uncertainties for bone tissue [36,44], in order to choose the optimal NS, the precision was evaluated for NS from 10 to 150 voxels (equivalent to 104 to 1560 µm), in steps of 10 voxels. A masked image of the preloaded (Preloaded1) or loaded (Loaded1) tibia (without the fibula) was generated by using the image processing and segmentation tools available in MATLAB (the MathWorks, Inc.) for the tests performed on the preloaded or loaded repeated images, respectively. A custom-made MATLAB (the MathWorks, Inc.) script was used to eliminate all the points of the grid not belonging to the bone. After this filter, all the cells of the DVC grid with at least one node within the bone mask were kept. All the remaining nodes of the grid were then converted into 8-node hexahedron elements with the respective computed displacements as kinematic boundary conditions. A finite element (FE) software package (ANSYS, Mechanical APDL v.15.0, Ansys, Inc, USA) was used to compute in each node of the DVC grid the components of the strain tensor, the first (tension, ε_{p1}) and third (compression, ε_{p3}) principal strains, and the average of the absolute values of the six components of the Cauchy's infinitesimal strain tensor (ε_m), as proposed in the literature [37,39]. The entire workflow is shown in Fig. 2. Table 1 summarises all the registrations performed on the sample.

2.3. Comparisons and statistics

Two different analyses were performed in this study:

(1) Precision and accuracy of the DVC for the whole mice tibia as a function of different NS in preloaded and loaded conditions for *in situ* samples. Repeated images from the *in situ*

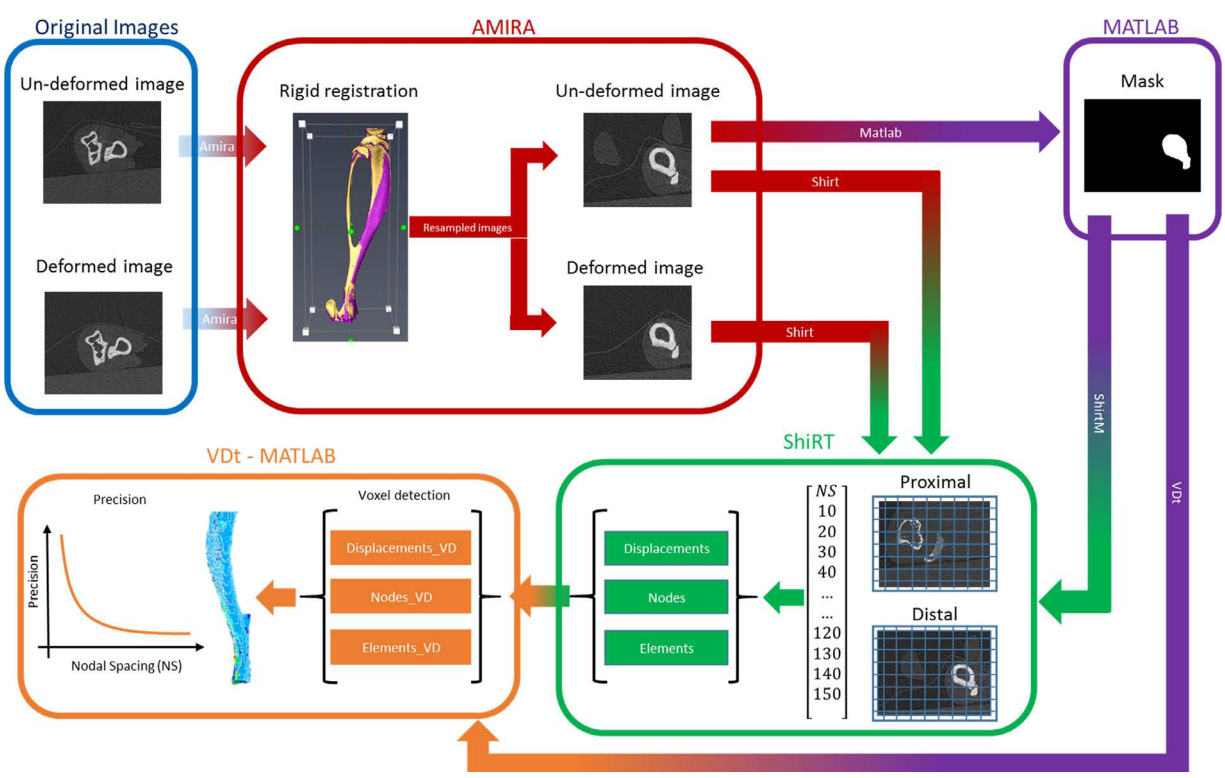

Fig. 2. Schematic representation of the entire workflow used for all the analysis. Two pair of images (un-deformed and deformed) are given as input (blue box) to Amira software where the rigid registration is computed (red box). The new resample pair of images are then given as input to ShiRT (green box) as well as a mask of the un-deformed image generated by Matlab (purple box). The output from ShiRT as well as the un-deformed mask are given as input to the Voxel Detection Toolkit (VDt). VDt remove all the voxels not included in the mask providing the strains information of the region of interest only.

Table 2.
Mean and standard deviation of the nodal values of principal tensile (ε_{p1}) and compressive (ε_{p3}) strain for Reg1, Reg2 and Reg3. Mean, standard deviation and range of the differences between the nodal values of principal tensile (ε_{p1}) and compressive (ε_{p3}) strain for Reg1 *vs.* Reg2 (Reg1/Reg2), and for Reg1 *vs.* Reg3 (Reg1/Reg3). For these analyses the DVC cells with the centroid within the whole bone mask were included. Results are reported for each specimen.

Sample	*Reg1*	*Reg2*	*Reg3*	*Reg1/Reg2*	*Range*	*Reg1/Reg3*	*Range*
Mean for each registration and differences between registrations for Min Principal Strain (ε_{p3}) [με]							
Specimen1	−13,919 ± 6701	−13,646 ± 6835	−16,971 ± 7616	−273 ± 890	−4179/2074	3052 ± 5526	−9666/17,144
Specimen2	−10,919 ± 4573	−9824 ± 4588	−8839 ± 4522	−1096 ± 625	−3632/670	−2080 ± 2554	−9537/4725
Specimen3	−16,882 ± 5673	−16,789 ± 5827	−19,267 ± 7422	−93 ± 875	−1996/2187	2385 ± 6076	−8676/17,246
Differences in Max Principal Strain (ε_{p1}) [με]							
Specimen1	9387 ± 5524	9131 ± 5686	13,813 ± 7703	256 ± 742	−2428/4016	−4427 ± 5649	−20,392/8561
Specimen2	10,195 ± 4164	12,199 ± 4335	10,880 ± 4334	−2004 ± 836	−4946/157	−686 ± 3146	−10,423/8664
Specimen3	10,286 ± 5891	10,111 ± 6067	14,127 ± 8898	174 ± 722	−1582/2048	−3842 ± 5805	−18,461/8352

Table 3.
Mean and standard deviation of the nodal values of principal tensile (ε_{p1}) and compressive (ε_{p3}) strain for Reg1, Reg2 and Reg3. Mean, standard deviation and range of the differences between the nodal values of principal tensile ($\varepsilon_p 1$) and compressive (ε_{p3}) strain for Reg1 *vs.* Reg2 (Reg1/Reg2), and for Reg1 *vs.* Reg3 (Reg1/Reg3). For these analyses the DVC cells with the centroid within the top (Proximal), middle (Mid-Shaft) or bottom (Distal) third of the tibia were included. Results are reported for each specimen.

Region	*Sample*	*Reg1*	*Reg2*	*Reg3*	*Reg1/Reg2*	*Range*	*Reg1/Reg3*	*Range*
Mean for each registration and differences between registrations for Min Principal Strain (ε_{p3}) [με]								
Proximal	Specimen1	−18,772 ± 6649	−18,526 ± 6941	−23,207 ± 6844	−247 ± 808	−2723/1219	4434 ± 3822	−8395/13,518
Proximal	Specimen2	−12,268 ± 3423	−11,223 ± 3489	−12,216 ± 3804	−1046 ± 564	−2189/670	−52 ± 1504	−4308/4725
Proximal	Specimen3	−22,380 ± 3437	−22,514 ± 3589	−26,749 ± 3658	133 ± 640	−1150/1598	4369 ± 3187	−3544/9759
Mid-shaft	Specimen1	−14,369 ± 3975	−14,519 ± 3614	−14,253 ± 6642	150 ± 982	−3075/2074	−116 ± 5184	−9666/14,792
Mid-shaft	Specimen2	−8534 ± 4294	−7504 ± 4347	−6283 ± 3749	−1031 ± 571	−2372/172	−2252 ± 2324	−9537/1584
Mid-shaft	Specimen3	−16,825 ± 2970	−17,004 ± 2390	−14,801 ± 7335	178 ± 1057	−1514/2187	−2025 ± 5234	−8676/9177
Distal	Specimen1	−8615 ± 4804	−7893 ± 4634	−13,452 ± 4978	−722 ± 622	−4179/387	4837 ± 5942	−8557/17,144
Distal	Specimen2	−11,954 ± 4935	−10,744 ± 4923	−8018 ± 3800	−1210 ± 717	−3632/−144	−3937 ± 2093	−9393 ± /1028
Distal	Specimen3	−11,447 ± 4070	−10,848 ± 3943	−16,310 ± 3748	−600 ± 637	−1996/982	4862 ± 6664	−6197/17,246
Differences in Max Principal Strain (ε_{p1}) [με]								
Proximal	Specimen1	15,181 ± 4879	15,408 ± 4804	20,575 ± 7816	−227 ± 646	−2428/1826	−5394 ± 5052	−20,392/4468
Proximal	Specimen2	12,092 ± 3965	13,828 ± 4263	12,458 ± 4796	−1737 ± 666	−3285/−554	−366 ± 3343	−10,423/6361
Proximal	Specimen3	16,712 ± 5385	17,131 ± 5129	22,460 ± 8890	−419 ± 525	−1582/709	−5748 ± 4894	−18,461/1294
Mid-shaft	Specimen1	7568 ± 2660	7251 ± 2302	7329 ± 4207	317 ± 661	−1112/3320	239 ± 3647	−10,866/8561
Mid-shaft	Specimen2	7505 ± 3013	9695 ± 3287	7325 ± 1898	−2190 ± 696	−3887/−773	179 ± 2357	−4593/5006
Mid-shaft	Specimen3	7354 ± 2200	7012 ± 1865	6079 ± 2847	341 ± 578	−511/1964	1275 ± 2605	−5928/8352
Distal	Specimen1	5411 ± 2832	4734 ± 2526	13,534 ± 3405	676 ± 626	−1206/4016	−8124 ± 4551	−18,000/3150
Distal	Specimen2	10,988 ± 3999	13,073 ± 4243	12,858 ± 3303	−2085 ± 1035	−4946/157	−1870 ± 3300	−7335/8664
Distal	Specimen3	6782 ± 2930	6188 ± 2607	13,910 ± 4115	594 ± 640	−778/2048	−7128 ± 5475	−18,403/1433

scans for both preloaded (0.5 N, later referred to as "RegP", Table 1) and loaded (13 N, later referred to as "RegL", Table1) conditions were registered and the following statistics were computed: the standard deviation of the error (SDER, [40]) as the standard deviation of the ε_m values at each measurement points; the mean absolute error (MAER, [40]) as the mean of the ε_m values at each measurement points. SDER and MAER were reported as a function of the different NS considered. Power laws were fitted between the medians of the values for the different samples and the NS. Standard deviations are reported in the figures as error bars and coefficients of determination (R^2) were computed for each power law. These analyses estimated the relationship between DVC uncertainties and NS in loaded conditions.

(2) Variability of the strain distribution in the mouse tibia if the hind-limb is repositioned in the testing machine imposing the same axial load. Preloaded and loaded images (before and after repositioning) from the *in situ* scans were registered with a NS equal to 50 voxels. Each tibia was cut below the growth plate in its proximal part, and below the attachment point with the fibula in its distal part. For each registration ε_{p1} and ε_{p3} were computed in each node. To evaluate the differences between the considered registrations (Reg1 between the second preloaded scan and the first loaded scan *vs.* Reg2, between the second preloaded scan and the second loaded scan, and *vs.* Reg3, between the second preloaded scan and the loaded scan after repositioning; Table1) for each specimen the following parameters were computed:
- mean and standard deviation of the nodal values ε_{p3} or ε_{p1} for each registration (Reg1, Reg2, Reg3) for the whole specimens (Table2);
- mean, standard deviation and range of the difference between the nodal values ε_{p3} or ε_{p1} computed for registration Reg1 and Reg2 (Reg1/Reg2, Table2) or for registration Reg1 and Reg3 (Reg1/Reg3, Table2), for the whole specimen;
- mean and standard deviation of the nodal values ε_{p3} or ε_{p1} for each registration (Reg1, Reg2, Reg3) for the top (Proximal), middle (Mid-Shaft) and bottom (Distal) thirds of the specimen according to their axial position (Table 3);
- mean, standard deviation and range of the difference between the nodal values ε_{p3} or ε_{p1} computed for registration Reg1 and Reg2 (Reg1/Reg2, Table3) or for the registration Reg1 and Reg3 (Reg1/Reg3, Table3), for the top (Proximal), middle (Mid-Shaft) and bottom (Distal) thirds of the specimen according to their axial position (Table3).

In order to avoid peaks of differences outside the bone region for this analysis, the cells of the DVC grid with centroid within the bone mask were included. These measurements of strain distribution on the mouse tibiae estimated the effect of repositioning *in vivo* if the leg is loaded with the same axial compressive load.

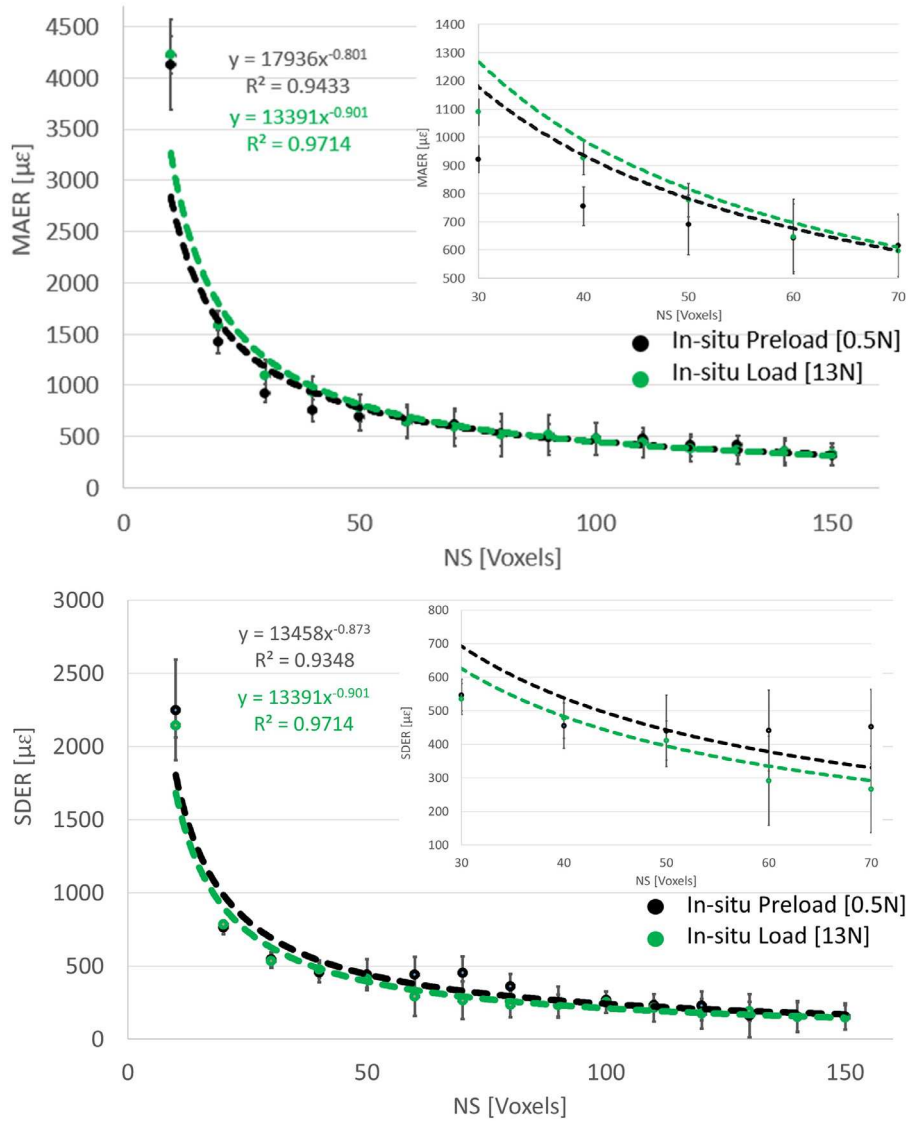

Fig. 3. Median of the standard deviation of the error (SDER) and of the mean absolute error (MAER) for *in situ* preloaded (black, $N = 3$) and *in situ* loaded (green, $N = 3$) conditions. Data are reported for the different tested nodal spacing (NS). Error bars represent standard deviations.

3. Results

3.1. DVC precision and accuracy for loaded condition for in situ analyses

The results show, as expected, a strong power relationship between both MAER and SDER with respect to the NS (MAER: $R^2 = 0.943$ for "*in situ* preloaded" and $R^2 = 0.971$ for "*in situ* loaded" images, respectively; SDER: $R^2 = 0.934$ for "*in situ* preloaded" and $R^2 = 0.971$ for "*in situ* loaded" images, respectively) with lower SDER for higher NS (Fig. 3). The DVC applied to *in situ* scans showed a SDER for preloaded and loaded conditions equal to 2249 ± 344με and 2144 ± 82με respectively, for NS of 10 voxels, to 440 ± 105με and 411 ± 58με for NS equal to 50 voxels, and of 156 ± 90με and 147 ± 81με for NS equal to 150 voxels (Fig. 3). For NS equal to 50 voxels homogeneous patterns of the error were found as reported for other bone structures [41,45].

3.2. Strain distribution before and after repositioning

Results from the strain distribution within the tibia measured twice with DVC on the whole leg loaded at the same level, without repositioning showed similar, but not identical strain distributions for all three specimens analysed (Figs. 4 and 5). Before repositioning, the ranges of the mean differences for first and third principal strains for the three specimens were −2004 to 256με and −1096 to −93με, respectively (Table 2). Larger differences in strain distributions were found after repositioning, with ranges of the mean differences for first and third principal strains for the three specimens of −4427 to −686με and −2080 to 3052με, respectively (Table 2). In addition, frequency plots for all registrations (before repositioning: Reg1, Reg2; after repositioning: Reg3) show, for specimen 1 and 3, a shift of the first and third principal strains after repositioning (Fig. 6).

The strain distribution for each registration and the differences in strain distributions before and after repositioning showed to be different from the different analysed sub-regions (Table3). In particular, for all specimens during the first and second loading (Reg1 and Reg2, before repositioning) the principal strains were higher in the most proximal part of the tibia compared to those in the midshaft and in the distal part. Differences between the strain distributions before repositioning (Reg1/Reg2) were similar for the three regions. Conversely, differences between the strain distributions after repositioning (Reg1/Reg3) were different for the sub-regions,

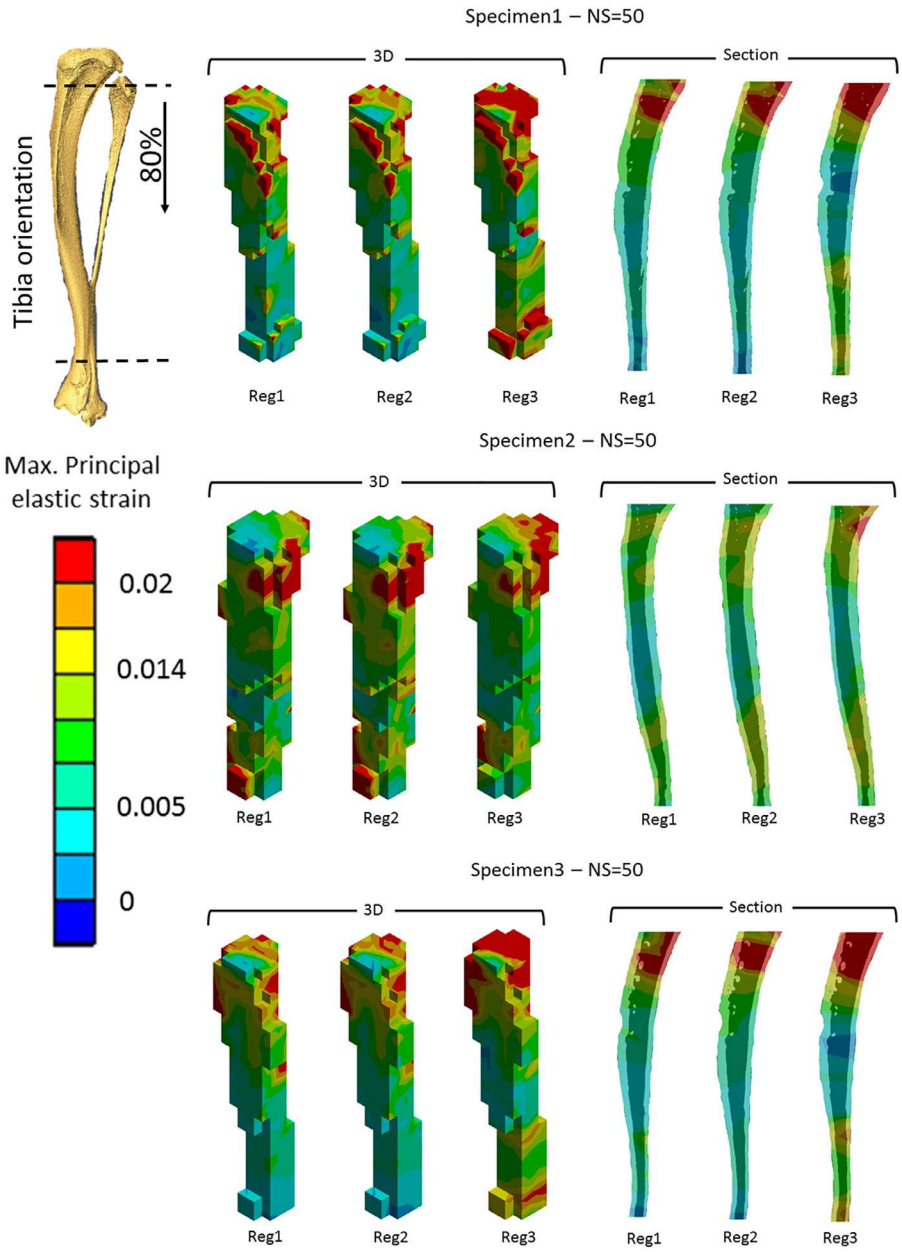

Fig. 4. Variability of the first principal strain (ε_{p1}) distribution within the tibia measured with DVC on whole leg loaded at the same compressive axial load level (13 N) without (Reg1: Preloaded2 *vs.* Loaded1; Reg2: Preloaded2 *vs.* Loaded2) and after repositioning (Reg3: Preloaded2 *vs.* Repositioned) for three different specimens. Results, obtained with a NS equal to 50 voxels, are shown for the 3D volume (left, for this visualization the DVC cells with at least one node within the bone mask were included), and for a longitudinal section (right, the strain distributions obtained from the registrations were overlapped with a mask of the longitudinal section of the same tibia. These analyses were conducted for a sub-sample of the tibiae (80% of the tibia calculated from just below the proximal growth plate).

highlighting that the effect of the repositioning affected the loading condition the specimens were subjected to.

4. Discussion

The aim of this study was to investigate the full field strain distribution within the mouse tibia induced by typical loading conditions applied during *in vivo* loading experiments of the mouse hind-limb, by using a combination of *in situ* mechanical testing, µCT scanning and a global DVC approach. In particular, the precision of the DVC method in loaded conditions, and the effect of repositioning on the strain distributions were evaluated.

One of the limitations of the previous studies that evaluated the precision of DVC is that unloaded images (zero-strain) were used [37,41]. However, it is interesting to understand its precision when the specimens are subjected to loading. The results of this study showed that the MAER and the SDER computed from *in situ* pairs of repeated preloaded (0.5 N compression) or loaded (13 N compression) images was very similar, therefore confirming that this DVC approach is robust according to the considered input images.

In vivo experiments on female C57BL/6 mice with single element strain gauges (sensor area lower then 2 mm^2) attached to the medial surface of the tibial diaphysis, showed averaged strains of up to 2000$\mu\varepsilon$ when axially loaded at 12 N with the *in vivo* tibia model. Moreover, when similar experiments were performed using DIC (with 12 N axial load), peaks of 5000$\mu\varepsilon$ were found in the same region (anterior-medial side) of the mouse tibia [26]. Considering that the diameter of the tibia is between 1000 µm and 2000 µm along its axis, the DVC method can be used to classify regions above and below such a limit, only for NS of

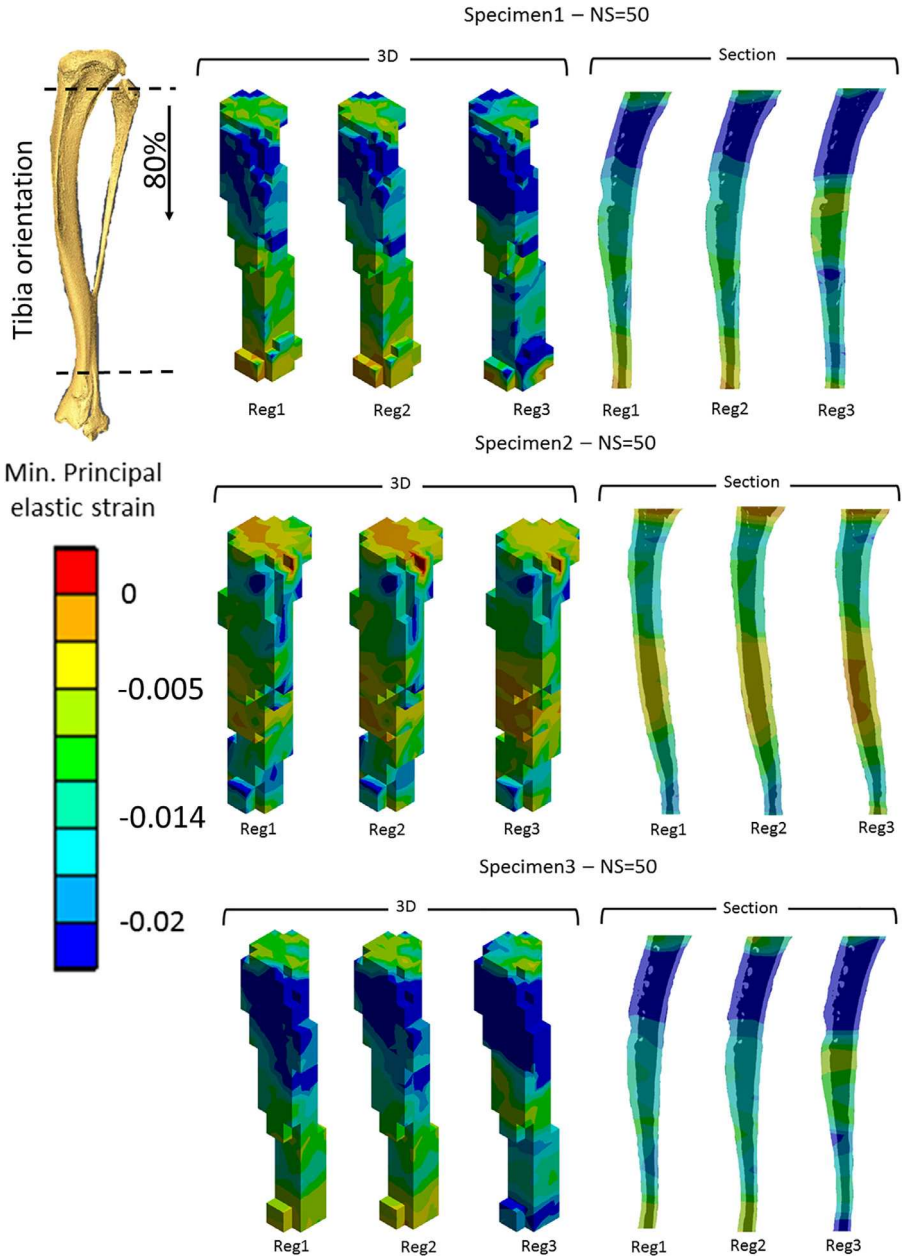

Fig. 5. Variability of the third principal strain (ε_{p3}) distribution within the tibia measured with DVC on whole leg loaded at the same compressive axial load level (13 N) without (Reg1: Preloaded2 *vs.* Loaded1; Reg2: Preloaded2 *vs.* Loaded2) and after repositioning (Reg3: Preloaded2 *vs.* Repositioned) for three different specimens. Results, obtained with a NS equal to 50 voxels, are shown for the 3D volume (left, for this visualization the DVC cells with at least one node within the bone mask were included), and for a longitudinal section (right, the strain distributions obtained from the registrations were overlapped with a mask of the longitudinal section of the same tibia. These analyses were conducted for a sub-sample of the tibiae (80% of the tibia calculated from just below the proximal growth plate).

approximately 50 voxels, which provides reasonable uncertainties for both *in situ* preloaded (440 ± 105με), and *in situ* loaded (411 ± 58με for NS equal to 50 voxels, equivalent to 520 μm) conditions (see Supplementary material for *ex vivo* and *in vivo* analyses). Indeed, this measurement spatial resolution is enough to evaluate heterogeneous strain localisation within the tibia along both longitudinal and transverse directions, but it cannot provide an heterogeneous map of strains within the single bone structural units (lamellae in the cortex or single trabeculae) for which higher image resolution is needed [46].

When pairs of microCT images acquired in the preloaded (Preloaded2) and loaded (Loaded1 or Loaded2) conditions without repositioning were registered, similar strain patterns were observed for all specimens (Figs. 4 and 5 – Reg1, Reg2) with mean differences below 2000με. In case of Specimen2 these values were higher than the estimated uncertainties of the measurement estimated in zero-strain or constant strain (due to image noise, rigid registration and interpolation, which were below 510με), showing a potential effect of the heterogeneous strain distribution on the precision of the method. Both distribution and magnitude of strains were similar but not identical, probably due to the intrinsic characteristics of the tested specimens such as size and shape, bone microstructure, and due to the variability in boundary conditions. Nevertheless, the strain distribution showed larger differences in specific regions of the bone (for example the distal end for Specimen1 and Specimen3) after repositioning (Figs. 4 and 5 – Reg3; Table3). Moreover, in this case, higher tensile and compressive principal strains in similar regions of the tibia were reported

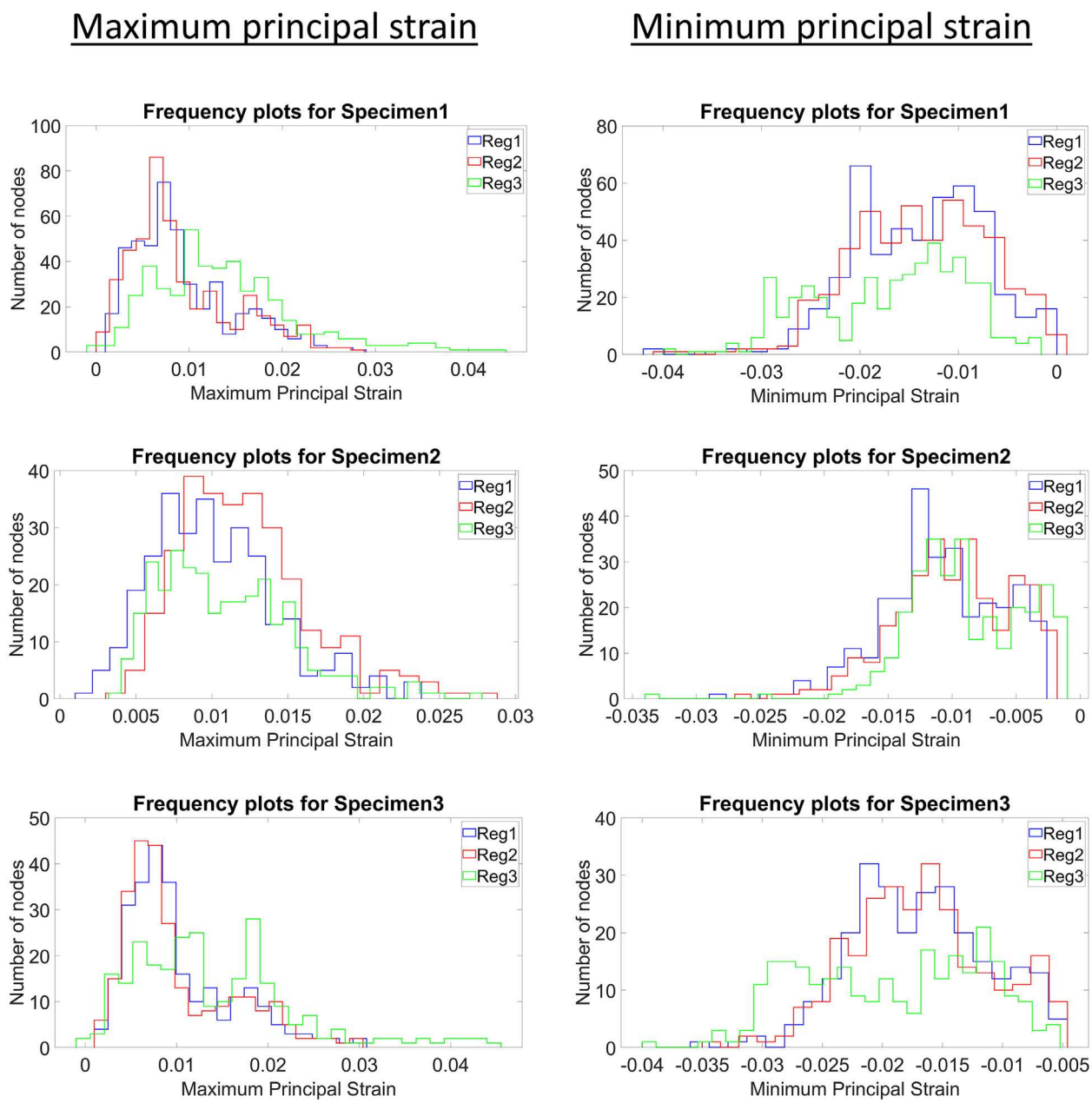

Fig. 6. Frequency plots without (Reg1: Preloaded2 *vs.* Loaded1; Reg2: Preloaded2 *vs.* Loaded2) and after repositioning (Reg3: Preloaded2 *vs.* Repositioned) of both first and third principal strain for the three different specimens.

(Figs. 4 and 5). This is also underlined by the large mean differences between the strain before and after repositioning (−4427 to −686με in first principal strain and −2080 to 3052με in third principal strain, compared to mean differences in the range of −2004 to 256με without repositioning) and highlights the possible variability induced by the repositioning in the *in vivo* loading experiments. Furthermore, big differences between differences in strain distributions were found after repositioning for the different subregions (Table3). The variability of the strain is probably due to the different loading conditions applied to the tibia through the tissues of the joint when the hind-limb is repositioned. Small differences in the repositioning can lead to large transverse loads at the knee and ankle that induce bending on the tibia, which could be only partially compensated for by the fibula. While this variability is not necessarily deleterious when studying the effect of a spectrum of loading scenarios on bone remodelling [11,47], it should be accounted for in case computational models are compared to experimental results [10,48–50].

Finite element models could be used to evaluate the effect of different boundary conditions on the internal strains within the mouse tibia, with a measurement spatial resolution even higher than DVC. However, since the current experimental approaches are not accurate enough to have a proper validation of the 3D internal strain field, these models have not been quantitatively validated for the prediction of strain. Moreover, the assignment of realistic boundary conditions in the FE models is not trivial due to the fact that in the *in vivo* tibia loading model, only the axial load between the knee and ankle joint is controlled, leaving undetermined the actual boundary conditions on the tibia. This limitation can be overcome with DVC measurements. Digital image correlation (DIC) is also intensively used to evaluate the strain distribution during loading. However, this approach is restricted to

measurements in a portion of the external surface of the bone, missing the potential of exploring the strain distribution within the bone, driven by the density and morphology of the underneath structures.

This study has a number of limitations. Results obtained on the analysis of the strain distribution from the repositioning were based on a limited number of specimens due to the large number of scans performed and the time needed to post-process the data. Only two of the three tested specimens behaved very similarly when distributions of strains were compared before and after repositioning, underlying some intrinsic variability among specimens. Therefore, in order generalize the findings and to provide a database consisting of a possible spectrum of loading conditions on the mouse tibia, induced by loading of the hind-limb, a larger number of specimens will be tested in the future. Secondly, the variability in strain due to repositioning found in this study is related to the specific endcaps used in our *in vivo* loading protocol. Different loading procedures may lead to lower or larger variability of the strain distribution, but the approach presented in this study can be used to quantify them with minor adaptations of the loading jig. Thirdly, the quasi-static compression required to perform stepwise loading during the µCT scans is driven by a loading rate which is much lower than the one used *in vivo* loading. Moreover, comparisons with strain gauges or DIC were not performed. The former would have created local artefacts in the µCT images that would have affected the DVC measurement, and the latter because with the current set-up was impossible to fit the DIC system inside the µCT device. Finally, one DVC approach was used for this study. Nevertheless, researchers are welcome to contact the corresponding author who will share the data used in this study for comparing different methods or download them from https://doi.org/10.15131/shef.data.7058078.

In conclusion, this study presents an approach to evaluate the full field strain distribution within the mouse tibia induced by a typical loading condition applied during *in vivo* loading experiments of the mouse hind-limb. These preliminary results have shown that the DVC approach applied to the mouse tibia can be precise enough to evaluate local deformations with a spatial resolution of approximately 500 µm. Furthermore, the repositioning of the hind-limb within the testing machine can induce large differences in the strain distributions that should be accounted for when evaluating mechano-regulated bone remodelling (*e.g.,* bone changes in a region) and comparing the results with computational models (*e.g.*, strain energy density or strain level in a certain region of the bone). This variability, which is probably due to the different (transverse) loading conditions applied to the tibia through the joints when the hind-limb is repositioned, suggests that an approach including stochasticity in the assignement of the boundary conditions in the FE models may lead to more realistic results. In addition, this method can be used to optimise the design of the mechanical plugs used in the *in vivo* loading tests in order to reduce the variability to a minumum.

Acknowledgements

The authors gratefully acknowledge Simon Rawson and John Wilson for manufacturing the jig, Prof David Barber and Prof Rod Hose for sharing the ShIRT library, Prof Timothy M Skerry for his thoughtful suggestions, Dr Gareth Fletcher for implementing the DVC service, the skelet.AL facility for access to the scanning facilities, Maya Boudiffa for her help with the µCT scanning, Sara Oliviero for her help with the Amira software, and Frederick Greatrex for proofreading the manuscript.

This study was partially funded by the FP7 European program MAMBO (PIEF-GA-2012327357), by the EPSRC (MultiSim project code EP/K03877X/1) and by the UK National Centre for the Replacement, Refinement and Reduction of Animals in Research (NC3Rs, grant number NC/R001073/1).

Ethical approval

All procedures were approved by the local Research Ethics Committee of the University of Sheffield (Sheffield, UK).

Competing interests

Authors have no conflict of interest associated to this paper.

Supplementary materials

Supplementary material associated with this article can be found, in the online version, at doi:10.1016/j.medengphy.2018.09.001.

References

[1] Carter DR. Mechanical loading histories and cortical bone remodeling. Calcified Tissue Int 1984;36:S19–24.
[2] Barak MM, Lieberman DE, Hublin J-J. A Wolff in sheep's clothing: trabecular bone adaptation in response to changes in joint loading orientation. Bone 2011;49:1141–51.
[3] Giorgi M, Verbruggen SW, Lacroix D. In silico bone mechanobiology: modeling a multifaceted biological system. Wiley Interdiscipl Rev Syst Biol Med 2016;8:485–505.
[4] Christen P, Ito K, Ellouz R, Boutroy S, Sornay-Rendu E, Chapurlat RD, et al. Bone remodelling in humans is load-driven but not lazy. Nat Commun 2014;5:4855.
[5] Schulte FA, Ruffoni D, Lambers FM, Christen D, Webster DJ, Kuhn G, et al. Local mechanical stimuli regulate bone formation and resorption in mice at the tissue level. PLoS One 2013;8:e62172.
[6] Sugiyama T, Price JS, Lanyon LE. Functional adaptation to mechanical loading in both cortical and cancellous bone is controlled locally and is confined to the loaded bones. Bone 2010;46:314–21.
[7] Nowlan NC, Chandaria V, Sharpe J. Immobilized chicks as a model system for early-onset developmental dysplasia of the hip. J Orthop Res: Off Publ Orthop Res Soc 2014;32:777–85.
[8] Comellas E, Carriero A, Giorgi M, Pereira A, Shefelbine SJ. Chapter 2 – modeling the influence of mechanics on biological growth. Numerical methods and advanced simulation in biomechanics and biological processes. Academic Press; 2018. p. 17–35.
[9] Giorgi M, Carriero A, Shefelbine SJ, Nowlan NC. Mechanobiological simulations of prenatal joint morphogenesis. J Biomech 2014;47:989–95.
[10] Pereira AF, Javaheri B, Pitsillides A, Shefelbine S. Predicting cortical bone adaptation to axial loading in the mouse tibia. J R Soc Interface 2015;12:20150590.
[11] Birkhold AI, Razi H, Duda GN, Weinkamer R, Checa S, Willie BM. Mineralizing surface is the main target of mechanical stimulation independent of age: 3D dynamic *in vivo* morphometry. Bone 2014;66:15–25.
[12] Birkhold AI, Razi H, Weinkamer R, Duda GN, Checa S, Willie BM. Monitoring *in vivo* (re)modeling: a computational approach using 4D microCT data to quantify bone surface movements. Bone 2015;75:210–21.
[13] Holguin N, Brodt MD, Sanchez ME, Kotiya AA, Silva MJ. Adaptation of tibial structure and strength to axial compression depends on loading-history in both C57BL/6 and BALB/C Mice. Calcified Tissue Int 2013;93:211–21.
[14] Oliviero S, Giorgi M, Dall'Ara E. Validation of Finite Element models of the mouse tibia using digital volume correlation. J Mech Behav Biomed Mater 2018.
[15] Hoshi A, Watanabe H, Chiba M, Inaba Y. Effects of exercise at different ages on bone density and mechanical properties of femoral bone of aged mice. Tohoku J Exp Med 1998;185:15–24.
[16] Leppänen OV, Sievänen H, Jokihaara J, Pajamäki I, Kannus P, Järvinen TL. Pathogenesis of age-related osteoporosis: impaired mechano-responsiveness of bone is not the culprit. PLoS One 2008;3:e2540.
[17] Fritton J, Myers E, Wright T, Van der Meulen M. Loading induces site-specific increases in mineral content assessed by microcomputed tomography of the mouse tibia. Bone 2005;36:1030–8.
[18] Lynch ME, Main RP, Xu Q, Walsh DJ, Schaffler MB, Wright TM, et al. Cancellous bone adaptation to tibial compression is not sex dependent in growing mice. J Appl Physiol 2010;109:685–91.
[19] Moustafa A, Sugiyama T, Prasad J, Zaman G, Gross T, Lanyon L, et al. Mechanical loading-related changes in osteocyte sclerostin expression in mice are more closely associated with the subsequent osteogenic response than the peak strains engendered. Osteoporos Int 2012;23:1225–34.
[20] Sugiyama T, Meakin LB, Browne WJ, Galea GL, Price JS, Lanyon LE. Bones' adaptive response to mechanical loading is essentially linear between the low strains associated with disuse and the high strains associated with the lamellar/woven bone transition. J Bone Min Res 2012;27:1784–93.

[21] Yang H, Embry RE, Main RP. Effects of loading duration and short rest insertion on cancellous and cortical bone adaptation in the mouse tibia. PLoS One 2017;12:e0169519.
[22] Patel TK, Brodt MD, Silva MJ. Experimental and finite element analysis of strains induced by axial tibial compression in young-adult and old female C57Bl/6 mice. J Biomech 2014;47:451–7.
[23] De Souza RL, Matsuura M, Eckstein F, Rawlinson SC, Lanyon LE, Pitsillides AA. Non-invasive axial loading of mouse tibiae increases cortical bone formation and modifies trabecular organization: a new model to study cortical and cancellous compartments in a single loaded element. Bone 2005;37:810–18.
[24] Torcasio A, Zhang X, Duyck J, van Lenthe GH. 3D characterization of bone strains in the rat tibia loading model. Biomech Model Mechanobiol 2012;11:403–10.
[25] Grassi L, Isaksson H. Extracting accurate strain measurements in bone mechanics: A critical review of current methods. J Mech Behav Biomed Mater 2015;50:43–54.
[26] Carriero A, Abela L, Pitsillides AA, Shefelbine SJ. Ex vivo determination of bone tissue strains for an *in vivo* mouse tibial loading model. J Biomech 2014;47:2490–7.
[27] Yavari SA, van der Stok J, Weinans H, Zadpoor AA. Full-field strain measurement and fracture analysis of rat femora in compression test. J Biomech 2013;46:1282–92.
[28] Gillard F, Boardman R, Mavrogordato M, Hollis D, Sinclair I, Pierron F, et al. The application of digital volume correlation (DVC) to study the microstructural behaviour of trabecular bone during compression. J Mech Behav Biomed Mater 2014;29:480–99.
[29] Bay BK, Smith TS, Fyhrie DP, Saad M. Digital volume correlation: Three-dimensional strain mapping using X-ray tomography. Exp Mech 1999;39:217–26.
[30] Bremand F, Germaneau A, Doumalin P, Dupre J. Study of mechanical behaviour of cancellous bone by digital volume correlation and x-ray micro-computed tomography. In: Proceedings of eleventh international congress and exposition; 2008. p. 2–5.
[31] Zauel R, Yeni Y, Bay B, Dong X, Fyhrie DP. Comparison of the linear finite element prediction of deformation and strain of human cancellous bone to 3D digital volume correlation measurements. J Biomech Eng 2006;128:1–6.
[32] Chen Y, Dall'Ara E, Sales E, Manda K, Wallace R, Pankaj P, et al. Micro-CT based finite element models of cancellous bone predict accurately displacement once the boundary condition is well replicated: a validation study. J Mech Behav Biomed Mater 2017;65:644–51.
[33] Christen D, Levchuk A, Schori S, Schneider P, Boyd SK, Müller R. Deformable image registration and 3D strain mapping for the quantitative assessment of cortical bone microdamage. J Mech Behav Biomed Mater 2012;8:184–93.
[34] Hussein AI, Barbone PE, Morgan EF. Digital volume correlation for study of the mechanics of whole bones. Proc IUTAM 2012;4:116–25.
[35] Danesi V, Tozzi G, Cristofolini L. Application of digital volume correlation to study the efficacy of prophylactic vertebral augmentation. Clin Biomech 2016;39:14–24.
[36] Roberts BC, Perilli E, Reynolds KJ. Application of the digital volume correlation technique for the measurement of displacement and strain fields in bone: a literature review. J Biomech 2014;47:923–34.
[37] Palanca M, Cristofolini L, Dall'Ara E, Curto M, Innocente F, Danesi V, et al. Digital volume correlation can be used to estimate local strains in natural and augmented vertebrae: an organ-level study. J Biomech 2016;49:3882–90.
[38] Dall'Ara E, Barber D, Viceconti M. About the inevitable compromise between spatial resolution and accuracy of strain measurement for bone tissue: a 3D zero-strain study. J Biomech 2014;47:2956–63.
[39] Liu L, Morgan EF. Accuracy and precision of digital volume correlation in quantifying displacements and strains in trabecular bone. J Biomech 2007;40:3516–20.
[40] Lu Y, Boudiffa M, Dall'Ara E, Bellantuono I, Viceconti M. Evaluation of in-vivo measurement errors associated with micro-computed tomography scans by means of the bone surface distance approach. Med Eng Phys 2015;37:1091–7.
[41] Dall'Ara E, Barber D, Viceconti M. About the inevitable compromise between spatial resolution and accuracy of strain measurement for bone tissue: a 3D zero-strain study. J Biomech 2014;47:2956–63.
[42] Barber D, Hose D. Automatic segmentation of medical images using image registration: diagnostic and simulation applications. J Med Eng Technol 2005;29:53–63.
[43] Barber DC, Oubel E, Frangi AF, Hose D. Efficient computational fluid dynamics mesh generation by image registration. Med Image Anal 2007;11:648–62.
[44] Palanca M, Tozzi G, Cristofolini L, Viceconti M, Dall'Ara E. Three-dimensional local measurements of bone strain and displacement: comparison of three digital volume correlation approaches. J Biomech Eng 2015:137.
[45] Dall'Ara E, Peña-Fernández M, Palanca M, Giorgi M, Cristofolini L, Tozzi G. Precision of digital volume correlation approaches for strain analysis in bone imaged with micro-computed tomography at different dimensional levels. Front Mater 2017;4:31. doi:10.3389/fmats.2017.00031.
[46] Palanca M, Bodey AJ, Giorgi M, Viceconti M, Lacroix D, Cristofolini L, et al. Local displacement and strain uncertainties in different bone types by digital volume correlation of synchrotron microtomograms. J Biomech 2017;58:27–36.
[47] Birkhold AI, Razi H, Duda GN, Weinkamer R, Checa S, Willie BM. The influence of age on adaptive bone formation and bone resorption. Biomaterials 2014;35:9290–301.
[48] Birkhold AI, Razi H, Duda GN, Weinkamer R, Checa S, Willie BM. The periosteal bone surface is less mechano-responsive than the endocortical. Sci Rep 2016;6:23480.
[49] Razi H, Birkhold AI, Weinkamer R, Duda GN, Willie BM, Checa S. Aging leads to a dysregulation in mechanically driven bone formation and resorption. J Bone Miner Res: Off J Am Soc Bone Miner Res 2015;30:1864–73.
[50] Razi H, Birkhold AI, Zaslansky P, Weinkamer R, Duda GN, Willie BM, et al. Skeletal maturity leads to a reduction in the strain magnitudes induced within the bone: A murine tibia study. Acta Biomater 2015;13:301–10.